Comparison of Gap-Enhanced Raman Tags and Nanoparticle Aggregates with Polarization Dependent Super-Resolution Spectral SERS Imaging

Deben N. Shoup[1], Sanjun Fan[1], Mario Zapata-Herrera[2,3], Hannah C. Schorr[1], Javier Aizpurua[3,4,5], and Zachary D. Schultz[1,6]*

1. Department of Chemistry and Biochemistry, The Ohio State University, Columbus, Ohio 43210, USA
2. Center for Materials Physics in San Sebastián (CSIC-UPV/EHU), Donostia-San Sebastián 20018, ESP
3. Donostia International Physics Center, Donostia-San Sebastián 20018, ESP
4. Ikerbasque, Basque Foundation for Science, 48009 Bilbao, ESP
5. Department of Electricity and Electronics, University of the Basque Country UPV/EHU, ESP, 48940 Leioa, ESP
6. Comprehensive Cancer Center, The Ohio State University, Columbus, Ohio 43210, USA

* corresponding author email: schultz.133@osu.edu

Abstract

Strongly confined electric fields resulting from nanogaps within nanoparticle aggregates give rise to significant enhancement in surface-enhanced Raman scattering (SERS). Nanometer differences in gap sizes lead to drastically different confined field strengths, so much attention has been focused on the development and understanding of nanostructures with controlled gap sizes. In this work, we report a novel petal gap-enhanced Raman tag (GERT) consisting of bipyramid core and a nitrothiophenol (NTP) spacer to support the growth of hundreds of small petals and compare its SERS emission and localization to a traditional bipyramid aggregate. To do this, we used super resolution spectral SERS imaging that simultaneously captures the SERS images and spectra while varying the incident laser polarization. Intensity fluctuations inherent of SERS enabled super resolution algorithms to be applied which revealed sub-diffraction limited differences in the localization with respect to polarization direction for both particles. Interestingly, however, only the traditional bipyramid aggregates experienced a strong polarization dependence in their SERS intensity and in the plasmon-induced conversion of NTP to dimercaptoazobenzene (DMAB), which was localized with nanometer precision to regions of intense electromagnetic

fields. The lack of polarization dependence (validated through electromagnetic simulations) and surface reactions from the bipyramid-GERTs suggest that the emissions arising from the bipyramid-GERTs are less influenced by confined fields.

TOC Graphic

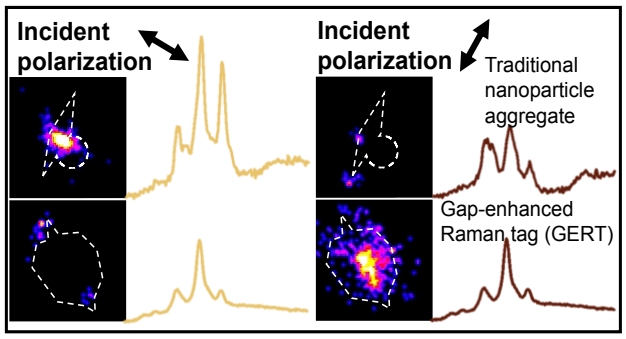

Introduction

The optical properties of gold nanoparticles have led to their popularity in a wide range of biological and physical sensing applications.[1-5] Their size-dependent localized surface plasmon resonance (LSPR) in the visible regime makes them particularly suited for optical microscopy and spectroscopies such as fluorescence and Raman scattering. Additionally, nanostructures illuminated with incident light near their LSPRs give rise to surface-enhanced plasmon spectroscopies due to the confined electric fields caused by LSPR generation.[6] Of particular importance is surface-enhanced Raman scattering (SERS), which takes advantage of the Raman signal enhancement resulting from the excitation of the LSPR and is capable of transforming Raman spectroscopy into a single-molecule or single-nanoparticle spectroscopy.[7-9] Nanogaps in nanoparticle aggregates cause greatly enhanced confined electric fields relative to single nanostructures, and these "hotspots" result in significant signal enhancement in SERS. The strong electric field confinement in these nanostructure systems also lead to the generation of hot carriers that can induce molecular and catalytic reactions on their surfaces, which can be readily monitored with SERS.[10-12]

Anisotropic nanoparticles , such as dimers, rods, bipyramids, stars, and core-satellites, enable stronger SERS enhancement relative to single nanospheres due to the intrinsic hotspots at gaps and sharp tips.[13-16] However, with anisotropic nanostructures, the polarization direction of linearly polarized incident light becomes important. For nanostructures with multiple plasmon resonances, the signal can alter drastically with polarization direction depending on the plasmon resonances relative to the excitation laser wavelength. In aggregated nanostructure systems, plasmon hybridization can occur, resulting in new plasmon modes not inherent of the individual structures forming the aggregate.[17, 18] These hybrid plasmon resonances are less predictable experimentally and can vary drastically from shape, size, orientation, and spacing of the structures forming the aggregate.[19-21]

An emerging class of nanostructures for SERS is gap-enhanced Raman tags (GERTs), where a reporter molecule, such as nitrothiophenol (NTP), is used as a shape directing agent to form size controlled nanogaps.[22, 23] A variety of GERTs have since been reported, but tend to fall into two distinct categories: smooth-shell GERTs (S-GERTs) that have a smooth outer shell and petal-GERTs (P-GERTs) that consist of small petal-like structures that create a roughened outer layer.[24] Generally, because of the large surface areas for molecules to adsorb and that the size of the gaps

can be easily controlled, both types of GERTs have been shown to have consistent and reliable particle-to-particle SERS responses.[25-27] However, because the P-GERTs have more nanogaps and a larger surface area for more reporter molecules to be immobilized on the surface, both of which are dependent on the number and size of petals, they tend to have brighter, more consistent SERS intensity, up to two orders of magnitude.[24, 28] P-GERTs and other spikey surfaced GERTs have mostly been limited to spherical or rod shaped cores.[28] The electric field confinement of GERTs, particularly P-GERTs, is generally less understood relative to traditional aggregates due to the complexity and large amount of petals that make electromagnetic simulations difficult.

Also important in the development and understanding of consistent, highly enhancing nanogap-based nanostructures is the development of methods to characterize them with high spatial resolution. Methods to spatially characterize the orientation and anisotropy of anisotropic nanostructures include dark field scattering[29], calcite assisted localization,[30] and nonlinear optical microscopy.[31] However, understanding polarization dependent SERS emissions with high spatial resolution has been more limited. Isolated nanostructures readily experience SERS intensity fluctuations or blinking, enabling stochastic super resolution algorithms, such as stochastic optical reconstruction microscopy (STORM), to localize the SERS emission from the nanoparticles beyond the optical diffraction limit.[32-34] Super resolution SERS has been used for a variety of applications including localizing chemical transformations,[35] hotspot formation,[36, 37] cellular peptide-protein interactions,[38] and single molecule optical trapping.[39, 40] Polarization dependent orientation and dipole differentiation of gold nanorods using super resolution SERS has been demonstrated previously,[41] but without direct correlation to the spectral regime. Recently, our group has demonstrated a super-resolution spectral SERS imaging method where the Raman signal is split into a spatial and spectral domain.[42] This enables direct correlation of the spatial order of isolated nanoparticles to their spectral responses. This method has successfully been used to investigate and localize short lived species resulting from molecular reactions to the tips of gold nanostars, where the field confinement is expected to be most intense.[35, 43]

In the present study, we report novel P-GERTs with bipyramid cores and compare their SERS localizations, spectra, and intensities relative to the incident polarization to traditional bipyramid aggregates to elucidate how energy couples in the nanogaps within the structures. To do this, we employ spectral SERS imaging which enables direct correlation of changes in the SERS emission and localization with respect to polarization in both the spatial and spectral domains. The

localizations of both types of structures were compared to correlated electron microscopy images with good agreement. The reporter molecule used, NTP, has multiple roles within this work. First, it is the Raman reporter molecule for the bipyramids and the Raman reporter and shape directing agent for the bipyramid-GERTs. Second, NTP undergoes a plasmon induced crosslinking to form dimercaptoazobenzene (DMAB) that can be readily observed and monitored. The ability to SERS hotspot map is suggested by correlating the occurrence of the conversion of NTP to DMAB to the localized emission at each polarization of the bipyramid aggregates. The bipyramid P-GERTs are shown to behave much differently in their polarization dependent localization and spectral features compared to the traditional bipyramid-aggregates, suggesting that the SERS enhancement of the bipyramid P-GERTs is not as heavily influenced by the confined electric fields. Our results, validated through electromagnetic simulations, further suggest that the magnitude of the confined field impacts molecular reactions on the surface.

Methods

Materials

(1-hexadecyl)trimethyl ammonium bromide (CTAB), hydrogen tetrachloroaurate (III) hydrate ($HAuCl_4$), trisodium citrate, ascorbic acid, (1-hexadecyl)trimethyl ammonium chloride (CTAC), sodium borohydride ($NaBH_4$), silver nitrate ($AgNO_3$), hydrochloric acid (HCl), and nitrothiophenol (NTP) where purchased from Sigma-Aldrich and used as received.

Synthesis of gold bipyramids

Synthesis and characterization of gold bipyramids was modified from that previously reported.[44] Some of the bipyramids synthesized were used for imaging while some were used as the core of the bipyramid-GERTs. The bipyramids not used for GERT formation were functionalized by adding 200 μL NTP to 2 mL gold bipyramid solution prior to imaging. More detailed experimental protocol can be found in the SI.

Synthesis of gold bipyramid-GERTs

Gold bipyramid core GERTs were prepared using a modified method.[45] 16 mL 50 mM CTAC, 2 mL gold bipyramid solution, and 200 μL 2 mM NTP were added in sequence to a 100 mL round bottom flask. After 5 mins, 200 μL 10 mM $HAuCl_4$ was added into this flask under stirring at 1200 rpm, followed by the addition of 200 μL 100 mM ascorbic acid. Finally, the

bipyramid core GERTs were synthesized after overnight incubation in 37 °C water bath (VWR) and the NPs precipitated out at the bottom of tube.

Sample preparation for imaging

5 μL of nanoparticles were dropped onto an ITO coated coverslip. Once the nanoparticles were dried, a copper transmission electron microscopy TEM grid without carbon film (Electron Microscopy Sciences) was taped on top of the dry dropped nanoparticles for correlated spectral SERS imaging and scanning electron microscopy (SEM).

Polarization dependent spectral SERS imaging

Spectral SERS imaging was conducted using a homebuilt wide field inverted transmission Raman microscope that has been extensively described previously.[35, 42] More detailed experimental information can be found in the SI.

Electron Microscopy

SEM images were acquired using a Thermo Scientific Apreo scanning electron microscope operating in Mode 2 (Optiplan) with beam energies from 5-10 kV and beam currents from 50 pA-0.1 nA. The Trinity2 detector was used to detect secondary electrons. Samples were imaged as prepared, with the addition of copper tape for grounding purposes. SEM images were always taken after spectral SERS imaging. For transmission electron microscopy (TEM), a Tecnai 30 TEM was used operating with a 300 kV electron beam, 38 μA screen current, 100 μm selected area aperture, 40 μm objective area, and an Orius 2k camera.

FEM Modeling

The optical response of the gold bipyramid, bipyramid-GERT, and bipyramid with ellipsoidal core nanoparticles was obtained by obtaining the induced electromagnetic fields for each dielectric configuration within the finite element method (FEM) implemented in the commercial COMSOL Multiphysics software version 6.1 (COMSOL AB, Stockholm, Sweden). More detailed experimental information can be found in the SI.

Data analysis and processing

Image processing and analysis was done with ImageJ (NIH), spectral processing was done with Matlab (Mathworks, version R2021b), and STORM fittings and drift corrections were done with the ThunderSTORM ImageJ plugin.[46] An ImageJ plugin developed by the Cox group was used for Haar wavelet kernel (HAWK) image preprocessing and STORM image reconstruction.[47]

The HAWK levels used were 4 and 5 for the bipyramids and bipyramid-GERTs respectively, negative values were separated, and the output stacked was grouped temporally.

Results

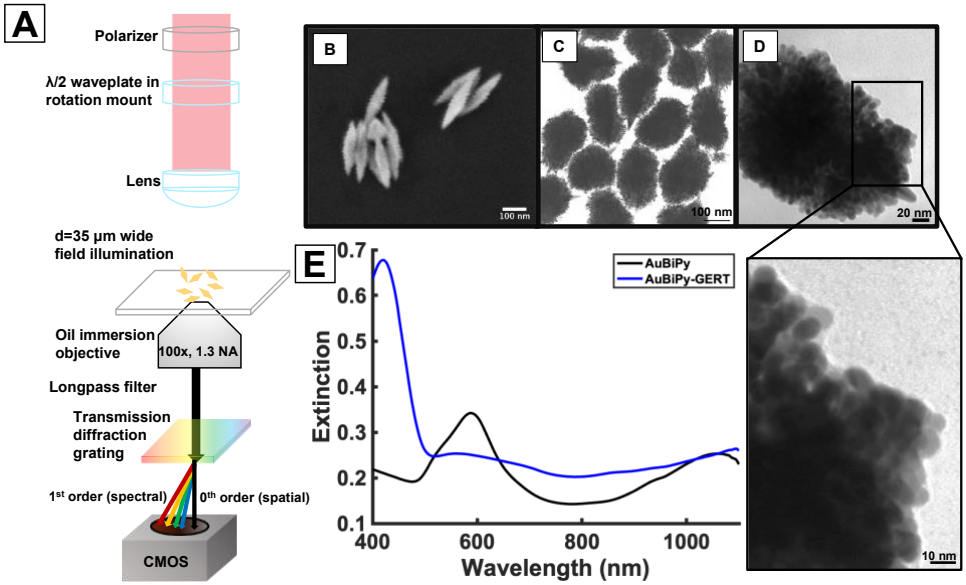

Figure 1. A) Instrument diagram of the spectral SERS microscope used for imaging. SEM images of the bipyramids (B) and TEM images of the bipyramid-GERTs (C and D). E) Ensemble extinction spectra for the bipyramids (black) and bipyramid-GERTs (blue).

The spectral SERS imaging microscope is illustrated in **Figure 1A**. This basic instrument has been extensively described previously,[35, 42] but a linear polarizer and **λ**/2 waveplate have been incorporated to control the polarization of the incident light for polarization-dependent imaging. The transmission diffraction grating placed prior to the imaging CMOS detector splits the signal into zeroth order diffraction (n=0) and first order diffraction (n=1) orders. The n=0 order contains the image while the n=1 order contains the spectral response; this enables direct and simultaneous

SERS imaging with correlation to the spectral regime. Electron microscopy images of the bipyramid and bipyramid-GERT nanoparticles used are shown in **Figure 1B-C**, respectively. The bipyramids have an average size length and width of 250 and 50 nm. The extinction spectrum for the bipyramid indicates that the ensemble latitudinal and longitudinal LSPRs are at 598 nm and 1060 nm (**Figure 1E**, black line). The formation of the GERTs onto the bipyramid (bipyramid-GERT) creates particles with layers of hundreds of 10 nm sized petals with numerous gaps between the high density of nanometer-sized petals that cover the surface **(Figure 1C and D)**. The GERT increases the average width of the nanostructure to 150 nm and significantly broadens the extinction spectrum (**Figure 1D**, blue line). For spectral imaging, the bipyramids were functionalized with a Raman reporter molecule, NTP, which was also used to facilitate the formation of the gaps within the GERT coating for the bipyramid-GERTs.[45]

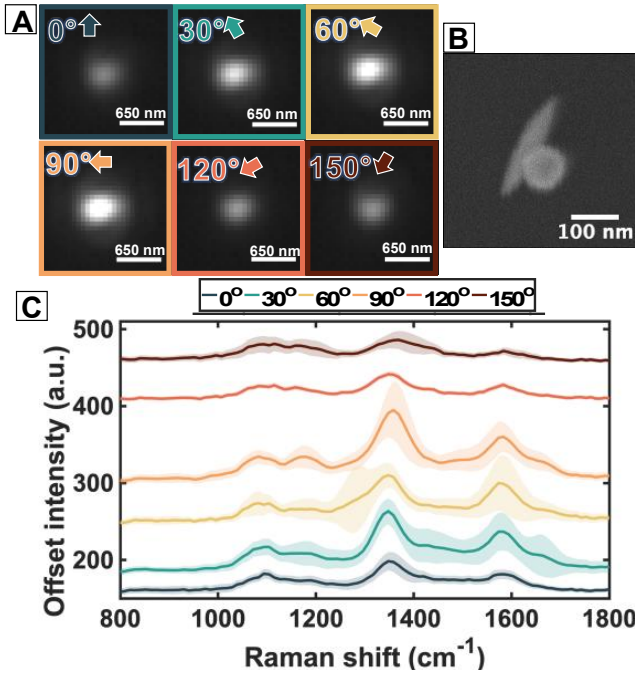

Figure 2. Polarization dependent spectral SERS imaging of a bipyramid-sphere aggregate functionalized with NTP. A) Average SERS image (n=0 diffraction order) and (B) SEM image of the chosen aggregate. The polarization angle and the direction of the polarization relative to the aggregate are indicated in the images in (A). C) Average SERS spectra (n=1 diffraction order) with shaded standard deviation of the aggregate in (A) and (B) at each polarization angle from 0-150°. The images in (A) have the same intensity scale. The power density of the excitation laser was 8 kW/cm^2 and 1000, 20 ms acquisitions were taken at each polarization angle.

To assess the polarization dependence of the SERS signal arising from these nanoparticles, the polarization angle of the incident light was rotated in 30° increments from 0-330°, and 1000 images were acquired at each polarization angle. It should be noted that single bipyramid particles were not detected at any incident polarization with the experimental conditions used. This was verified by correlating the field of view in the SERS image to SEM images of the same area, where single bipyramids are observed **(Figure S1)** in the SEM images but not in the SERS images at any polarization direction. This indicates that the bipyramids used in this study cannot be detected as single particles, but dimers and larger aggregates can be detected, which is consistent with prior work.[27, 48] Some of the bipyramids formed aggregates with spheres from the seed used to synthesize the bipyramids, which produced a strong polarization-dependent SERS signal, so this shape of aggregate provides a comparison to the bipyramid-GERTs. **Figure 2** shows polarization dependent imaging of a representative bipyramid-sphere aggregate (denoted BPA for brevity) from the first half-rotation of the polarization. The polarization dependent image and spectral intensity fluctuations from the BPA can be viewed in Video S1. The average point spread functions (psf) of the aggregate **(Figure 2A)** for each polarization angle show a clear change in intensity with polarization. A SEM image of the aggregate **(Figure 2B)** is shown to correlate the spectral SERS psf to the shape and orientation of the aggregate. Comparing the orientation of the nanoparticle in the SEM image **(Figure 2B)** and polarization of the incident light reveals that the scattering from the BPA is brightest when the incident light is oriented with the short axis of the bipyramid and orthogonally through the junction between the bipyramid and sphere (60^o and 90^o).

The average spectra of the same aggregate at each polarization angle are shown in **Figure 2C**, and the changes in intensity follow the same trend as in **Figure 2A**. In all the average spectra, three characteristic NTP bands at 1070, 1335, and 1580 cm^{-1} are present, but there are also peak shifts and additional peaks in the average spectra that also become evident in the shaded standard deviations. The standard deviations suggest the occurrence of intensity and frequency fluctuations that are lost in the average spectra. NTP undergoes a plasmon-driven catalytic conversion to a crosslinked product, dimercaptoazobenzene (DMAB)[49-51]; the peak shifts and additional peaks are consistent with DMAB formation. For example, at 90°, a band appears at 1156 cm^{-1} and the 1335 cm^{-1} peak is shifted to 1356 cm^{-1} while the bands at 1070 and 1580 cm^{-1} do not shift. Heat maps of all the individual collected spectra for each polarization angle **(Figure S2A)** show that the BPA experiences frequent spectral and intensity fluctuations throughout the measurement that follow

the same polarization dependence as the averaged intensities in the images. The average spectra and heatmaps for two additional BPAs **(Figure S3 and S4)** show the same polarization dependent behavior with frequent intensity fluctuations.

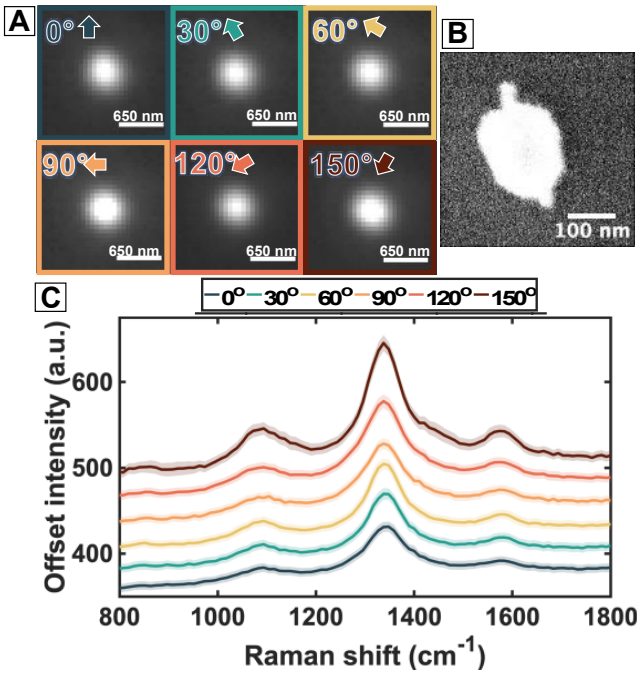

Figure 3. Polarization dependent spectral SERS imaging of a representative bipyramid-GERT. A) Average SERS image (n=0 diffraction order) and (B) SEM image of the same bipyramid-GERT. The polarization angle and the direction of the polarization relative to the nanoparticle is shown are indicated in the images in (A). C) Average SERS spectra (n=1 diffraction order) with shaded standard deviation of the nanoparticle in (A) and (B) at each polarization angle from 0-150°. The images in (A) have the same intensity scale. The power density of the excitation laser was 15 kW/cm^2 and 1000, 50 ms acquisitions were taken at each polarization angle.

Figure 3 shows spectral SERS imaging of a representative bipyramid-GERT nanoparticle (denoted BPG for brevity). The polarization dependent image and spectral intensity fluctuations from the BPG can be viewed in Video S2. In **Figure 3A**, the average intensity of the psf for the BPG **(Figure 3B)** at each polarization angle does not significantly vary with polarization angle. The SEM image of the BPG **(Figure 3B)** shows the ends of the bipyramid slightly protrude from the petals forming the GERT. Unlike the BPA shown in **Figure 2A**, the intensity of the average psf does not change significantly as the polarization of the incident laser is rotated. This indicates that the GERT coating prevents preferential scattering depending on the polarization and suggests that the bulk of the scattering arises from the GERT coating rather than the bipyramid core.

The average spectrum at each polarization angle for the BPG is shown in **Figure 3C**. No bands or peak shifts indicative of DMAB are observed. Heat maps showing all the collected spectra for each polarization angle **(Figure S2B)** and the small standard deviation shadings in Figure 3C show that the BPG spectra only change in intensity slightly when the polarization angle changes and that there are no spectra associated with DMAB in any of the spectra collected. This is consistent in the average spectra and heatmaps for two additional BPGs **(Figures S5 and S6)**. Therefore, the photocatalytic conversion of NTP to DMAB is not readily observed with the GERT coating on the bipyramid. It should also be noted that the BPGs were imaged with a higher laser power density and longer acquisition time (15 kW/cm^2 and 50 ms/frame acquisition rate) compared to the BPAs (8 kW/cm^2 and 20 ms/frame acquisition rate). Even at this higher laser power, the BPGs do not readily reduce NTP to DMAB. This change in power dependence suggests there are significant differences in the electric field resulting from these two types of nanostructures. Directly comparing the polarization dependence of the BPAs and BPGs (**Figure S7**) reveals that the BPAs experience polarization dependent intensity fluctuations while the BPGs do not experience strong intensity fluctuations and have a less consistent and weaker polarization dependence.

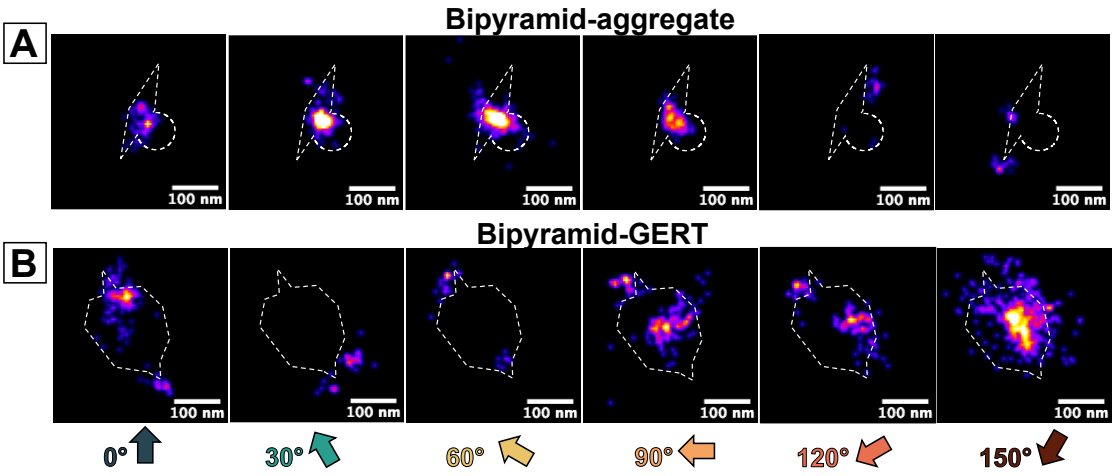

Figure 4. Super resolution images with HAWK pre-processing of the (A) BPA and (B) BPG from each polarization reveals differences between the types of particles. The outlined structures indicate the size and orientation of the nanostructures as determined by SEM. The arrows at the bottom indicate the polarization direction of the incident light. The scale bars are 100 nm.

The difference in polarization behavior suggests differences in the origin of the emission from the two types of particles that can be disentangled with localization microscopy. The reconstructed super resolution images using STORM are shown in **Figure S8A and S8B** for the BPA and the BPG, respectively. The emission for both particles emerges from the centers of the psfs and of the SEM-estimated position of the nanostructure. Using a single emitter fit when there is more than one emitter within one emitter per μm^2 can introduce image artifacts[52] and STORM can artificially create an ensemble averaged position for closely-spaced emitters that are up to 200 nm apart.[47] Separating these localizations by polarizations **(Figure S9)** reveals differences in location, frequency, and shape of the emissions for the BPA. However, only slight changes in shape for the BPG **(Figure S9C)** were observed where at polarizations along the bipyramid axis the localization is spherical while at polarizations through the GERT the localization is more ellipsoidal. To combat the mislocalization, Haar wavelet kernel (HAWK) pre-processing was conducted. HAWK effectively applies several bandpass filters that separates overlapping spots on the basis of the blinking behavior, and the final output is an image stack with more frames than the original, which enables more accurate localization.[47] While there are other methods for high density analysis, such as multi-emitter fitting in STORM, there are still drawbacks in localization resolution, image artifacts, and localization precision.[53-55] The reconstructed images from HAWK pre-processing followed by STORM of polarizations 0-150^o **(Figure S8C and S8D)** reveal emissions from multiple areas, rather than one in the center, for both types of particles.

Separating the localizations by polarization angle reveals differences in the signal origins with polarization. **Figure 4A and B** show the HAWK pre-processed super-resolved localization mapping of the BPA and the BPG, respectively, for each polarization from 0 to 150^o. The polarization dependent localization for the other two BPAs and BPGs are shown in **Figure S10 and S11,** respectively**.** For the BPA, the emission is localized to the junction between the bipyramid and sphere at the polarizations where the signal was greatest and intensity fluctuations occurred (30^o, 60^o, and 90^o). At the polarizations more along the long axis of the bipyramid (120^o and 150^o), the localization occurs near the tips or along the edges of the bipyramid rather than in the hotspot between then sphere and bipyramid. For the BPG, the emission localizes near the tips of the protruding bipyramid when the polarizations are along the long axis of the bipyramid in the area of the GERT for the polarizations through the widest part of the GERT coating. Interestingly, the

emission localizes differently with polarization even though the SERS signal arising from the GERT changes only slightly, but not consistently, with polarization.

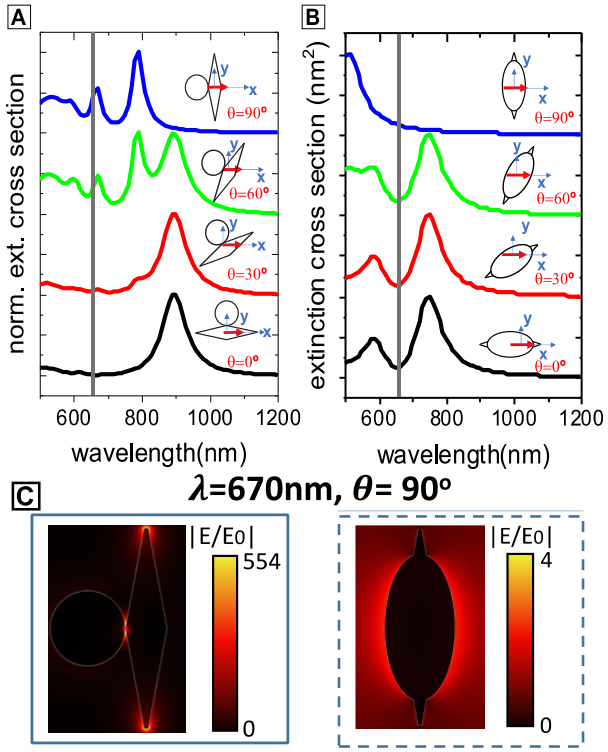

Figure 5. COMSOL FEM simulations of the extinction cross section for the (A) BPA and (B) BPG simplified with an ellipsoidal shell at various incident electric field orientations. The gray vertical line indicates the energy of the incident laser. C) FEM near-field calculations for the BPA (left) and BPG (right) with an incident wavelength of 670 nm and at the θ=90° polarization.

To further explain the origin of the signal and polarization dependence of the BPAs, the optical response of the aggregates at various polarizations were simulated using FEM to solve Maxwell's equations **(Figure 5A)**. The configurations used for the simulations are shown in **Figure S12.** The simulations keep the orientation of the electric field stable but change the orientation of the nanoparticle, θ. When the nanoparticle is oriented such that the electric field is propagating along the long axis of the bipyramid ($\theta = 0°$, black curve), which is where the signal is consistently the lowest for the BPAs discussed previously, there is a single peak in the simulated emission spectrum at 900 nm. When the nanoparticle is oriented such that the electric field is propagating along the short axis of the bipyramid and through the junction between the sphere and the bipyramid ($\theta = 90°$, blue curve), where the signal is consistently more intense for the BPAs discussed previously,

there are peaks in the emission spectrum at 675 and 800 nm. This is due to plasmon hybridization between the closely spaced bipyramid and sphere and results in significant enhancement of the signal when the 660 nm incident laser is oriented accordingly, as near field distribution plots show in **Figure S13**. The optical response of the bipyramids without the sphere (**Figure S14)** does not have a response near 675 nm and is similar to the experimental extinction spectrum of the bipyramids (**Figure 1E)**.

Due to the complexity and high density of the GERT coating on the BPG particles, the shape of the GERT coating was simulated simply by configuring a singular ellipsoidal shaped particle that is the same size and shape as the average GERT coating. This model captures the polarization dependent behavior observed. The simulated optical response **(Figure 5B)** of the ellipsoid-coated bipyramid has two longitudinal modes at 580 nm and 720 nm when the electric field is oriented orthogonal to the long axis of the bipyramid and in intermediate orientations ($\theta = 0, 30, 60°$) and a transverse mode at 520 nm. With this ellipsoid coated bipyramid, the excitation wavelength does not overlap with any of the modes in the simulated optical response, explaining the lack of polarization dependence in the SERS responses from the BPG particles and suggests quenching of the enhancement from the gaps in this structure.[56-58] This is further validated by the near-field simulations **(Figure 5C),** where at an excitation wavelength of 670 nm and θ=90° polarization, the BPA experiences a two order of magnitude greater near-field amplitude ($|E/E_0|$) than the BPG.

Discussion

Our results suggest that, using polarization dependent super-resolution spectral SERS imaging, we can further elucidate how energy couples between nanoparticles within different types of complex nanostructures. The BPGs used in this study lack polarization dependence similar to other bulky, petalled nanostructure geometries with large surface areas for molecules to adsorb.[59] In this study, the BPGs exhibit much more consistent particle-to-particle signal compared to the BPAs (**Figure 4A**), and the lack of polarization dependence in the spectral response suggests that the SERS signal is independent of the orientation of the nanostructures. These results are consistent with electromagnetic calculations of the plasmonic modes involved in the optical response, which show polarization-dependent spectral activity of the hybridized bipyramids-sphere system near the incident laser wavelength (660 nm), whereas no relevant modes are identified at that spectral range from an effective modeling of the BPGs. However, super resolution SERS indicated that there is

some polarization dependence the emission origin from the particle, but the spectral response appears to be independent of whether the emission originates from the center or the ends of the nanostructures.

It is interesting to note that the BPAs in this study consistently experience higher SERS intensity compared to the BPGs **(Figure S7)** when SERS enhancement factors (SERS EF) of GERTs have been reported to be comparable or higher than traditional aggregates.[28] This suggests that the bipyramid-GERTs experience different electric fields and are not as influenced by plasmonic coupling as the bipyramid-sphere aggregates **(Figure 5)**. The high density of petals causing small gaps within the center of the GERTs could be responsible for damping the electromagnetic enhancement. In traditional aggregate or nanogap-based nanoparticle systems, decreasing the gap size between nanoparticle aggregates increases the SERS EF, but once the gap size moves into the sub-nanometer to contact range, enhancement is limited by charge transfer and the SERS intensity subsequently decreases.[60] A similar phenomenon has been observed in studies using GERTs. In traditional GERTs, where an internal nanogap separates a spherical core and shell, the SERS intensity has been shown to decrease with gaps less than 2 nm.[61] P-GERTs with less than 10 large (>10 nm) petals have a higher SERS intensity compared to P-GERTs with hundreds of small (<5 nm) petals.[45] This has also been observed with similar aggregated, gapped nanostructure geometries.[62] It is possible that the lower than expected SERS enhancement is due to the high number of petals within the GERT layer on the bipyramid, and future optimization of the number and size of the petals within the GERT may provide increased signals.

In contrast to the BPGs, the BPAs experiences much greater and frequent intensity fluctuations, even at the incident polarizations that result in the weakest signal intensity. This suggests that the BPGs do not experience as strongly confined fields as two particles. The BPAs showed evidence of DMAB formation while the BPGs did not; however, the formation of DMAB was not consistent from aggregate-to-aggregate. Of the three BPAs analyzed, only one had consistent DMAB formation throughout the measurement, one has some DMAB formation at the expected polarizations, and one did not show any evidence of DMAB formation. The photocatalytic conversion of NTP to DMAB is well characterized and considered a model catalytic reaction with SERS[63, 64], but the measurements are often in the bulk or with microparticles rather than on the single or isolated-aggregated nanoparticle level, which limits the structural information that can be obtained. It has been shown that a homogenous distribution of traditional gold

nanoparticles results in heterogenous catalytic activity where only a fraction of nanostructures are responsible for the dimerization of NTP to DMAB.[65] Previously, tip-enhanced Raman spectroscopy (TERS) was used to study this reaction on single nanoprisms where the reduction predominately occurred along the edges and corners of the nanostructures.[66, 67] For these two BPAs where the photocatalytic reaction is occurring, the DMAB formation is strongest at polarizations where the plasmon hybridization is occurring **(Figure 5)** and when the emission is localized to the junction between the bipyramid and the sphere. Our results suggest an alternative imaging method to monitor reactions on nanostructures and localize where the reaction is occurring.

Conclusions

In conclusion, we describe novel bipyramid-shaped GERT (BPG) particles and compare their polarization dependent SERS emissions and photocatalytic conversion of NTP to DMAB to traditional aggregates containing bipyramids (BPA) using spectral super-resolution SERS imaging. Our results show that the BPG nanostructures do not experience a strong polarization dependence in the Raman spectra, and these nanostructures showed no evidence of the photocatalytic conversion of NTP to DMAB. The BPAs do experience a polarization dependence in the intensity and frequency of SERS intensity fluctuations, supported by FEM simulations. Comparing the SERS spectra to the localization at each polarization suggests that the photocatalytic conversion of NTP to DMAB occurs more readily in the junction within the aggregate, and the occurrence is dependent on the incident polarization, suggesting the ability to hotspot map. The culmination of this work also suggests that the petalled GERT structure is not as heavily influenced by the confined fields relative to a traditional aggregate and the importance of confined field strength on molecular reactions on nanostructured surfaces.

ASSOCIATED CONTENT

Supporting Information

Experimental details for nanobipyramid synthesis, spectral SERS imaging, and FEM modeling; SEM and SERS correlation example; spectral characterization, localization, and polarization dependence of additional nanoparticles; comparison of STORM with and without HAWK; COMSOL configurations and near field simulations; FEM modeling of nanobipyramids; videos showing fluctuations of BPAs and BPGs.

ACKNOWLEDGMENT

Electron microscopy was performed at the Center for Electron Microscopy and Analysis (CEMAS) at The Ohio State University. The authors thank Brian Scarpitti and Abigail Smith for TEM. The work was funded by an award from the National Science Foundation CHE- 2107791 to ZDS. MZ and JA acknowledge funding from project IT1526-22 from the Department of Education of the Basque Government, and from grant PID2022-139579NB-I00 funded by MCIN/AEI/10.13039/501100011033 and by "ERDF A way of making Europe".

References

1. Bansal, S. A.; Kumar, V.; Karimi, J.; Singh, A. P.; Kumar, S., Role of gold nanoparticles in advanced biomedical applications. *Nanoscale Adv.* **2020,** *2* (9), 3764-3787.
2. Chang, C.-C.; Chen, C.-P.; Wu, T.-H.; Yang, C.-H.; Lin, C.-W.; Chen, C.-Y., Gold nanoparticle-based colorimetric strategies for chemical and biological sensing applications. *Nanomaterials* **2019,** *9* (6), 861.
3. Xiao, T.; Huang, J.; Wang, D.; Meng, T.; Yang, X., Au and Au-Based nanomaterials: Synthesis and recent progress in electrochemical sensor applications. *Talanta* **2020,** *206*, 120210.
4. Zhang, J.; Mou, L.; Jiang, X., Surface chemistry of gold nanoparticles for health-related applications. *Chem. Sci.* **2020,** *11* (4), 923-936.
5. Yuan, Z.; Hu, C.-C.; Chang, H.-T.; Lu, C., Gold nanoparticles as sensitive optical probes. *Analyst* **2016,** *141* (5), 1611-1626.
6. Willets, K. A.; Van Duyne, R. P., Localized surface plasmon resonance spectroscopy and sensing. *Annu. Rev. Phys. Chem.* **2007,** *58*, 267-297.
7. Krug, J. T.; Wang, G. D.; Emory, S. R.; Nie, S., Efficient Raman enhancement and intermittent light emission observed in single gold nanocrystals. *J. Am. Chem. Soc.* **1999,** *121* (39), 9208-9214.
8. Kneipp, K.; Wang, Y.; Kneipp, H.; Perelman, L. T.; Itzkan, I.; Dasari, R. R.; Feld, M. S., Single molecule detection using surface-enhanced Raman scattering (SERS). *Phys. Rev. Lett.* **1997,** *78* (9), 1667.
9. Xu, H.; Bjerneld, E. J.; Käll, M.; Börjesson, L., Spectroscopy of single hemoglobin molecules by surface enhanced Raman scattering. *Phys. Rev. Lett.* **1999,** *83* (21), 4357.
10. Sprague-Klein, E. A.; Negru, B.; Madison, L. R.; Coste, S. C.; Rugg, B. K.; Felts, A. M.; McAnally, M. O.; Banik, M.; Apkarian, V. A.; Wasielewski, M. R., Photoinduced plasmon-driven chemistry in trans-1, 2-bis (4-pyridyl) ethylene gold nanosphere oligomers. *J. Am. Chem. Soc.* **2018,** *140* (33), 10583-10592.
11. Zoltowski, C. M.; Lalisse, R. F.; Hadad, C. M.; Schultz, Z. D., Plasmonically generated tryptophan radical anion on gold nanoparticles investigated by combined surface-enhanced

Raman scattering and density functional theory calculations. *J. Phys. Chem. C* **2021,** *125* (50), 27596-27606.
12. Huang, Y.-F.; Zhu, H.-P.; Liu, G.-K.; Wu, D.-Y.; Ren, B.; Tian, Z.-Q., When the signal is not from the original molecule to be detected: chemical transformation of para-aminothiophenol on Ag during the SERS measurement. *J. Am. Chem. Soc.* **2010,** *132* (27), 9244-9246.
13. Halas, N. J.; Lal, S.; Chang, W.-S.; Link, S.; Nordlander, P., Plasmons in strongly coupled metallic nanostructures. *Chem. Rev.* **2011,** *111* (6), 3913-3961.
14. Hao, E.; Schatz, G. C.; Hupp, J. T., Synthesis and optical properties of anisotropic metal nanoparticles. *J. Fluoresc.* **2004,** *14*, 331-341.
15. Burrows, N. D.; Vartanian, A. M.; Abadeer, N. S.; Grzincic, E. M.; Jacob, L. M.; Lin, W.; Li, J.; Dennison, J. M.; Hinman, J. G.; Murphy, C. J., Anisotropic nanoparticles and anisotropic surface chemistry. *J. Phys. Chem. Lett.* **2016,** *7* (4), 632-641.
16. Wustholz, K. L.; Henry, A.-I.; McMahon, J. M.; Freeman, R. G.; Valley, N.; Piotti, M. E.; Natan, M. J.; Schatz, G. C.; Van Duyne, R. P., Structure− activity relationships in gold nanoparticle dimers and trimers for surface-enhanced Raman spectroscopy. *J. Am. Chem. Soc.* **2010,** *132* (31), 10903-10910.
17. Lee, H.; Kim, G.-H.; Lee, J.-H.; Kim, N. H.; Nam, J.-M.; Suh, Y. D., Quantitative plasmon mode and surface-enhanced Raman scattering analyses of strongly coupled plasmonic nanotrimers with diverse geometries. *Nano Lett.* **2015,** *15* (7), 4628-4636.
18. Prezgot, D.; Ianoul, A., Probing the anisotropy of SERS enhancement with spatially separated plasmonic modes in strongly coupled silver nanocubes on a dielectric substrate. *J. Phys. Chem. C* **2015,** *119* (6), 3293-3301.
19. Velleman, L.; Scarabelli, L.; Sikdar, D.; Kornyshev, A.; Liz-Marzán, L.; Edel, J., Monitoring plasmon coupling and SERS enhancement through in situ nanoparticle spacing modulation. *Faraday Discuss.* **2017,** *205*, 67-83.
20. Dreaden, E. C.; Near, R. D.; Abdallah, T.; Talaat, M. H.; El-Sayed, M. A., Multimodal plasmon coupling in low symmetry gold nanoparticle pairs detected in surface-enhanced Raman scattering. *Appl. Phys. Lett.* **2011,** *98* (18).
21. Romero, I.; Aizpurua, J.; Bryant, G. W.; De Abajo, F. J. G., Plasmons in nearly touching metallic nanoparticles: singular response in the limit of touching dimers. *Opt. Express* **2006,** *14* (21), 9988-9999.
22. Nam, J.-M.; Oh, J.-W.; Lee, H.; Suh, Y. D., Plasmonic nanogap-enhanced Raman scattering with nanoparticles. *Acc. Chem. Res.* **2016,** *49* (12), 2746-2755.
23. Qiu, Y.; Zhang, Y.; Li, M.; Chen, G.; Fan, C.; Cui, K.; Wan, J.-B.; Han, A.; Ye, J.; Xiao, Z., Intraoperative detection and eradication of residual microtumors with gap-enhanced Raman tags. *ACS Nano* **2018,** *12* (8), 7974-7985.
24. Zhang, Y.; Gu, Y.; He, J.; Thackray, B. D.; Ye, J., Ultrabright gap-enhanced Raman tags for high-speed bioimaging. *Nat. Commun.* **2019,** *10* (1), 3905.
25. Gu, Y.; Zhang, Y.; Li, Y.; Jin, X.; Huang, C.; Maier, S. A.; Ye, J., Raman photostability of off-resonant gap-enhanced Raman tags. *RSC Adv.* **2018,** *8* (26), 14434-14444.
26. Wang, S.; Liu, Z.; Bartic, C.; Xu, H.; Ye, J., Improving SERS uniformity by isolating hot spots in gold rod-in-shell nanoparticles. *J. Nanopart. Res.* **2016,** *18*, 1-11.
27. Scarpitti, B. T.; Fan, S.; Lomax-Vogt, M.; Lutton, A.; Olesik, J. W.; Schultz, Z. D., Accurate Quantification and Imaging of Cellular Uptake Using Single-Particle Surface-Enhanced Raman Scattering. *ACS Sens.* **2023**.

28. Khlebtsov, N. G.; Lin, L.; Khlebtsov, B. N.; Ye, J., Gap-enhanced Raman tags: fabrication, optical properties, and theranostic applications. *Theranostics* **2020,** *10* (5), 2067.
29. Koen, K. A.; Weber, M. L.; Mayer, K. M.; Fernandez, E.; Willets, K. A., Spectrally-resolved polarization anisotropy of single plasmonic nanoparticles excited by total internal reflection. *J. Phys. Chem. C* **2012,** *116* (30), 16198-16206.
30. Monaghan, J. W.; O'Dell, Z. J.; Sridhar, S.; Paranzino, B.; Sundaresan, V.; Willets, K. A., Calcite-Assisted Localization and Kinetics (CLocK) Microscopy. *J. Phys. Chem. Lett.* **2022,** *13* (45), 10527-10533.
31. Steves, M. A.; Knappenberger Jr, K. L., Distinguishing Single-Metal Nanoparticles with Subdiffraction Spatial Resolution Using Variable-Polarization Fourier Transform Nonlinear Optical Microscopy. *Chem. Biomed. Imaging* **2023,** *1* (1), 91-98.
32. Willets, K. A.; Wilson, A. J.; Sundaresan, V.; Joshi, P. B., Super-resolution imaging and plasmonics. *Chem. Rev.* **2017,** *117* (11), 7538-7582.
33. Jin, D.; Xi, P.; Wang, B.; Zhang, L.; Enderlein, J.; van Oijen, A. M., Nanoparticles for super-resolution microscopy and single-molecule tracking. *Nat. Methods* **2018,** *15* (6), 415-423.
34. Tang, M.; Han, Y.; Jia, D.; Yang, Q.; Cheng, J.-X., Far-field super-resolution chemical microscopy. *Light: Sci. Appl.* **2023,** *12* (1), 137.
35. de Albuquerque, C. D. L.; Zoltowski, C. M.; Scarpitti, B. T.; Shoup, D. N.; Schultz, Z. D., Spectrally Resolved Surface-Enhanced Raman Scattering Imaging Reveals Plasmon-Mediated Chemical Transformations. *ACS Nanosci. Au* **2021,** *1* (1), 38-46.
36. de Albuquerque, C. D. L.; Hokanson, K. M.; Thorud, S. R.; Sobral-Filho, R. G.; Lindquist, N. C.; Brolo, A. G., Dynamic imaging of multiple SERS hotspots on single nanoparticles. *ACS Photonics* **2020,** *7* (2), 434-443.
37. Willets, K. A., Super-resolution imaging of SERS hot spots. *Chem. Soc. Rev.* **2014,** *43* (11), 3854-3864.
38. de Albuquerque, C. D. L.; Schultz, Z. D., Super-resolution surface-enhanced Raman scattering imaging of single particles in cells. *Anal. Chem.* **2020,** *92* (13), 9389-9398.
39. Kitahama, Y.; Funaoka, M.; Ozaki, Y., Plasmon-enhanced optical tweezers for single molecules on and near a colloidal silver nanoaggregate. *J. Phys. Chem. C* **2019,** *123* (29), 18001-18006.
40. Liang, L.; Zheng, P.; Zhang, C.; Barman, I., A Programmable DNA-Silicification-Based Nanocavity for Single-Molecule Plasmonic Sensing. *Adv. Mater.* **2021,** *33* (7), 2005133.
41. Wang, M.; Chen, M.; Zhanghao, K.; Zhang, X.; Jing, Z.; Gao, J.; Zhang, M. Q.; Jin, D.; Dai, Z.; Xi, P., Polarization-based super-resolution imaging of surface-enhanced Raman scattering nanoparticles with orientational information. *Nanoscale* **2018,** *10* (42), 19757-19765.
42. Shoup, D. N.; Scarpitti, B. T.; Schultz, Z. D., A Wide-Field Imaging Approach for Simultaneous Super-Resolution Surface-Enhanced Raman Scattering Bioimaging and Spectroscopy. *ACS Meas. Sci. Au* **2022,** *2* (4), 332-341.
43. Zoltowski, C. M.; Shoup, D. N.; Schultz, Z. D., Investigation of SERS Frequency Fluctuations Relevant to Sensing and Catalysis. *J. Phys. Chem. C* **2022,** *126* (34), 14547-14557.
44. Li, Q.; Zhuo, X.; Li, S.; Ruan, Q.; Xu, Q.-H.; Wang, J., Production of Monodisperse Gold Nanobipyramids with Number Percentages Approaching 100% and Evaluation of Their Plasmonic Properties. *Advanced Optical Materials* **2015,** *3* (6), 801-812.
45. Khlebtsov, B. N.; Burov, A. M.; Bratashov, D. N.; Tumskiy, R. S.; Khlebtsov, N. G., Petal-like Gap-Enhanced Raman Tags with Controllable Structures for High-Speed Raman Imaging. *Langmuir* **2020,** *36* (20), 5546-5553.

46. Ovesný, M.; Křížek, P.; Borkovec, J.; Švindrych, Z.; Hagen, G. M., ThunderSTORM: a comprehensive ImageJ plug-in for PALM and STORM data analysis and super-resolution imaging. *Bioinformatics* **2014,** *30* (16), 2389-2390.
47. Marsh, R. J.; Pfisterer, K.; Bennett, P.; Hirvonen, L. M.; Gautel, M.; Jones, G. E.; Cox, S., Artifact-free high-density localization microscopy analysis. *Nat. Methods* **2018,** *15* (9), 689-692.
48. Pardehkhorram, R.; Bonaccorsi, S.; Zhu, H.; Gonçales, V. R.; Wu, Y.; Liu, J.; Lee, N. A.; Tilley, R. D.; Gooding, J. J., Intrinsic and well-defined second generation hot spots in gold nanobipyramids versus gold nanorods. *Chem. Commun.* **2019,** *55* (53), 7707-7710.
49. Ren, X.; Tan, E.; Lang, X.; You, T.; Jiang, L.; Zhang, H.; Yin, P.; Guo, L., Observing reduction of 4-nitrobenzenthiol on gold nanoparticles in situ using surface-enhanced Raman spectroscopy. *Phys. Chem. Chem. Phys.* **2013,** *15* (34), 14196-14201.
50. van Schrojenstein Lantman, E. M.; Deckert-Gaudig, T.; Mank, A. J.; Deckert, V.; Weckhuysen, B. M., Catalytic processes monitored at the nanoscale with tip-enhanced Raman spectroscopy. *Nat. Nanotechnol.* **2012,** *7* (9), 583-586.
51. Sun, M.; Zhang, Z.; Zheng, H.; Xu, H., In-situ plasmon-driven chemical reactions revealed by high vacuum tip-enhanced Raman spectroscopy. *Sci. Rep.* **2012,** *2* (1), 647.
52. Titus, E. J.; Willets, K. A., Superlocalization surface-enhanced Raman scattering microscopy: comparing point spread function models in the ensemble and single-molecule limits. *ACS Nano* **2013,** *7* (9), 8284-8294.
53. Lakadamyali, M., Super-resolution microscopy: Going live and going fast. *ChemPhysChem* **2014,** *15* (4), 630-636.
54. Gustafsson, N.; Culley, S.; Ashdown, G.; Owen, D. M.; Pereira, P. M.; Henriques, R., Fast live-cell conventional fluorophore nanoscopy with ImageJ through super-resolution radial fluctuations. *Nat. Commun.* **2016,** *7* (1), 12471.
55. Nehme, E.; Weiss, L. E.; Michaeli, T.; Shechtman, Y., Deep-STORM: super-resolution single-molecule microscopy by deep learning. *Optica* **2018,** *5* (4), 458-464.
56. Zhu, W.; Esteban, R.; Borisov, A. G.; Baumberg, J. J.; Nordlander, P.; Lezec, H. J.; Aizpurua, J.; Crozier, K. B., Quantum mechanical effects in plasmonic structures with subnanometre gaps. *Nat. Commun.* **2016,** *7* (1), 1-14.
57. Slaughter, L. S.; Wu, Y.; Willingham, B. A.; Nordlander, P.; Link, S., Effects of symmetry breaking and conductive contact on the plasmon coupling in gold nanorod dimers. *ACS Nano* **2010,** *4* (8), 4657-4666.
58. El-Khoury, P. Z.; Hu, D.; Apkarian, V. A.; Hess, W. P., Raman scattering at plasmonic junctions shorted by conductive molecular bridges. *Nano Lett.* **2013,** *13* (4), 1858-1861.
59. Li, Q.; Jiang, Y.; Han, R.; Zhong, X.; Liu, S.; Li, Z. Y.; Sha, Y.; Xu, D., High surface-enhanced Raman scattering performance of individual gold nanoflowers and their application in live cell imaging. *Small* **2013,** *9* (6), 927-932.
60. Zhu, W.; Crozier, K. B., Quantum mechanical limit to plasmonic enhancement as observed by surface-enhanced Raman scattering. *Nat. Commun.* **2014,** *5* (1), 5228.
61. Lin, L.; Zhang, Q.; Li, X.; Qiu, M.; Jiang, X.; Jin, W.; Gu, H.; Lei, D. Y.; Ye, J., Electron transport across plasmonic molecular nanogaps interrogated with surface-enhanced Raman scattering. *ACS Nano* **2018,** *12* (7), 6492-6503.
62. Shim, J.-E.; Kim, Y. J.; Choe, J.-H.; Lee, T. G.; You, E.-A., Single-Nanoparticle-Based Digital SERS Sensing Platform for the Accurate Quantitative Detection of SARS-CoV-2. *ACS Appl. Mater. Interfaces* **2022,** *14* (34), 38459-38470.

63. Xie, W.; Schlücker, S., Surface-enhanced Raman spectroscopic detection of molecular chemo-and plasmo-catalysis on noble metal nanoparticles. *Chem. Commun.* **2018,** *54* (19), 2326-2336.
64. Sambur, J. B.; Chen, P., Approaches to single-nanoparticle catalysis. *Annu. Rev. Phys. Chem.* **2014,** *65*, 395-422.
65. Zhang, Z.; Kneipp, J., Mapping the inhomogeneity in plasmonic catalysis on supported gold nanoparticles using surface-enhanced Raman scattering microspectroscopy. *Anal. Chem.* **2018,** *90* (15), 9199-9205.
66. Li, Z.; Wang, R.; Kurouski, D., Nanoscale photocatalytic activity of gold and gold–palladium nanostructures revealed by tip-enhanced raman spectroscopy. *J. Phys. Chem. Lett.* **2020,** *11* (14), 5531-5537.
67. Li, Z.; Kurouski, D., Elucidation of photocatalytic properties of gold–platinum bimetallic nanoplates using tip-enhanced Raman spectroscopy. *J. Phys. Chem. C* **2020,** *124* (23), 12850-12854.